This is a repository copy of *Topological quantum switching enabled neuroelectronic synaptic modulators for brain computer interface*.

White Rose Research Online URL for this paper:
https://eprints.whiterose.ac.uk/212301/

Version: Published Version

eprints@whiterose.ac.uk
https://eprints.whiterose.ac.uk/

Topological Quantum Switching Enabled Neuroelectronic Synaptic Modulators for Brain Computer Interface

Dani S. Assi, Hongli Huang, Vaithinathan Karthikeyan, Vaskuri C. S. Theja, Maria Merlyne de Souza, and Vellaisamy A. L. Roy**

Aging and genetic-related disorders in the human brain lead to impairment of daily cognitive functions. Due to their neural synaptic complexity and the current limits of knowledge, reversing these disorders remains a substantial challenge for brain–computer interfaces (BCI). In this work, a solution is provided to potentially override aging and neurological disorder-related cognitive function loss in the human brain through the application of the authors' quantum synaptic device. To illustrate this point, a quantum topological insulator (QTI) Bi_2Se_2Te-based synaptic neuroelectronic device, where the electric field-induced tunable topological surface edge states and quantum switching properties make them a premier option for establishing artificial synaptic neuromodulation approaches, is designed and developed. Leveraging these unique quantum synaptic properties, the developed synaptic device provides the capability to neuromodulate distorted neural signals, leading to the reversal of age-related disorders via BCI. With the synaptic neuroelectronic characteristics of this device, excellent efficacy in treating cognitive neural dysfunctions through modulated neuromorphic stimuli is demonstrated. As a proof of concept, real-time neuromodulation of electroencephalogram (EEG) deduced distorted event-related potentials (ERP) is demonstrated by modulation of the synaptic device array.

1. Introduction

Brain aging and memory are time-irreversible factors of human life, and evidence of their reversal via artificial neuromodulators has been consistently growing in recent years.[1] Challenging the advancements of supercomputers with human intelligence, the operational capacity of the human brain remains unsurprisingly superior in aspects of processing capacity, power, and speed.[2–5] Despite these exceptional characteristics, the impact of aging on the human brain significantly damages its major cognitive functions.[1,6–10] Age-related changes, such as a decrease in the number of neurons and neurotransmitter effectiveness, cause weakened synaptic strength and lead to major neurodegenerative disorders such as Alzheimer's disease, Parkinson's disease, and amnesic cognitive impairment.[1,11] Although there are no practical solutions to reverse these aging effects on the human brain, efforts are underway to develop an artificial synaptic neuromodulator as a brain–computer interface, with projects such as Neuralink being notable examples.[12] On the other hand, developing an artificial synaptic neuromodulator that matches the human brain's performance is highly complex, involving high energy consumption and poor parallel processing latency.[13] These drawbacks are attributed to the nature of active materials and respective device characteristics, whose response to electric stimuli is incompatible with that of the human brain.[14] Hence, understanding the synaptic neural process of the human brain and creating an optimal material and device design for handling synaptic neural events are of utmost importance.

The human brain, via the modulation of neural plasticity, marks events of learning or memorizing. Based on the plasticity of these events in neuron clusters, they are categorized into short-term memory (s to min) and long-term memory (h to days). The initiation of these neural plasticity modulations occurs via an applied electric stimulus, which is either a presynaptic potentiation pulse (+ve) or a depression pulse (−ve).[12,15–19] To characterize the efficacy of these events, Hebbian techniques such as paired-pulse facilitation/depression and post-tetanic potentiation/depression are used.[3,20–23] The interdependency of neuron cluster pathways greatly influences these efficacies; short-term plasticity (STP) is the major phenomenon that

D. S. Assi, V. Karthikeyan, V. A. L. Roy
School of Science and Technology
Hong Kong Metropolitan University
Ho Man Tin, Hong Kong China
E-mail: vkarthik@hkmu.edu.hk; vroy@hkmu.edu.hk
H. Huang
Electronics and Nanoscale Engineering
James Watt School of Engineering
University of Glasgow
Glasgow G12 8QQ, U.K.
V. C. S. Theja
Department of Mechanical Engineering
The University of Hong Kong
Pokfulam Road, Hong Kong China
M. M. de Souza
Electronics and Electrical Engineering
The University of Sheffield
Sheffield S3 7HQ, U.K.

**ADVANCED
SCIENCE NEWS**

www.advancedsciencenews.com

**ADVANCED
MATERIALS**

www.advmat.de

influences the stability of long-term plasticity (LTP), meaning that they exhibit a high paired-pulse facilitation (PPF) index.[24,25] Moreover, the ability to respond to potentiation/depression stimuli declines as a result of aging in the human brain.[1,7–10] Thus, to mimic these events, the specific design of artificial synapses and electronic neuromodulation is required to prevent aging-related diseases in humans.

Over the years, the field of neuromodulation has evolved significantly from traditional methods such as Deep Brain Stimulation to many innovative techniques via electromagnetic and genetic interface routes.[26,27] These advancements are particularly crucial in addressing complex health challenges, notably those related to neurological and cognitive impairments often induced by aging in the human brain.[28] Here, the electro-modulation of neural signals is pivotal in addressing a range of neurological disorders. Despite its efficacy for various conditions, the requirement for invasive electrode implantation is prone to failure due to tissue reactions and also faces challenges in achieving precision targeting.[29–32] In addition to traditional electrical approaches, advancements in neuromodulation include diverse techniques such as thermal, optical, chemical, acoustic, and magnetic modalities, which are often integrated with programmable, multi-modal systems.[28] In genetic neurostimulation, light, heat, or chemicals control neural activity by targeting neuron clusters to modify and express alterations in ion channels for initiating action. This positions them as powerful tools for high-resolution interrogation of specific cell types and neural circuits.[28,33–35] Despite its potential, these techniques face challenges in clinical application due to the complexity of genetic modification and the need for specialized light or chemical delivery systems.[36,37] Recently, demonstrations of sonogenetic modulation have replaced opto- and chemogenetics; however, further research is necessary to fully understand the behavioral outcomes of this modulation.[37,38] On the other hand, magneto-neural stimulation stands out as the most prevalent method for therapeutic use, especially in treating drug-resistant depression. However, its effectiveness is limited to neurons that lie close to the outer layer of the human brain, which restricts this technique's spatiotemporal precision and target selectivity.[39,40] Understanding these inherent merits and limitations underscores the prolonged need for the development of non-invasive modes of neuroelectronic modulators for enhanced brain–computer interfaces.

In this aspect, recent demonstrations of artificial synaptic neuroelectronic modulators have been exhibited using conventional CMOS-based memory devices, where the lack of synchronization with biological synapses complicated the learning–memorizing process.[13,14,41,42] Hence, to bridge this gap and improve performance, the development of a new class of semiconductor materials with exceptional switching/processing speed and sensitivity to ultra-low processing power is mandatory. Meeting these criteria, QTI materials possess electric field-induced tunable conduction at edge surface states,[43–48] which are ideal for neuromorphic artificial synaptic neuromodulation. Their exotic topological quantum properties, such as protected edge surface states and ultrafast carrier transport, are capable of supporting artificial synapse functions with a large PPF index.[49]

In this work, we report on the design and development of a QTI bismuth selenide telluride (Bi_2Se_2Te)-based synaptic neuro-

electronic device for treating neurological disorders and for neuroprosthetic applications. For the proof of concept, we demonstrate unique performance in the neuromodulation of brain signals as bidirectional communication for brain–computer interfaces in a more biologically plausible manner. By biomimicking the synaptic neural behavior of the human brain, we demonstrate the characteristic response of post-synaptic potentials (PSPs) in our Bi_2Se_2Te synaptic neuroelectronic device, where we prove the effective tuning of neural facilitation functions. Moreover, supported by the topological edge-state dependent quantum switching properties in our synaptic neuroelectronic device, we demonstrate the development of flexible tunable PPF/Paired Pulse Depression (PPD) index ranges. This flexible neuromodulation behavior, being reported for the first time, showcases precise control capacity in the learning-to-forgetting process of the human brain by shaping its electrophysiological activities. In addition, we demonstrate real-time neuromodulation of EEG derived event-related potentials of elderly individuals with cognitive dysfunctions for brain–computer interface applications. Our findings provide deep insights into the synchronization and memory function longevity in human brain performance, thereby mitigating the causes and impacts of aging and neurological disorders in human life.

2. Results and Discussion

2.1. Quantum Topological Synaptic Neuroelectronic Device Design

To fabricate the synaptic neuroelectronic device, an electrochemically optimized material design of Bi_2Se_2Te is deposited with silver top electrodes and fluorine-doped tin oxide serving as presynaptic and postsynaptic neural points, respectively, as shown in **Figure 1a**. QTI materials represent a novel class of semiconducting materials characterized by edge state electronic transport properties that are immune to the backscattering of charges and feature adjustable narrow bandgap edges. These properties of topological insulator materials arise from their insulating bulk and conducting surface states, leading to ultralow switching threshold voltage requirements.[50] Matching the requirements for low power and high switching speed, QTIs are the material of choice for the fabrication of synaptic neuroelectronic devices. Figure 1a–g displays the materials characteristics and analysis of the Bi_2Se_2Te thin film; detailed characteristics of the developed thin films are shown in Figures S1–S3, Supporting Information.

The quantum switching performance of the synaptic devices is investigated by their change in device resistance states, obtained from *I–V* characteristics. The mechanism involved in the switching process is illustratively represented in **Figure 2a**, where the surface edge states of Bi_2Se_2Te with a band gap are demonstrated. The initial surface edge states in Bi_2Se_2Te demonstrate a quantum resistance level of $\sim h/e^2$, which, under the influence of an exerted internal electric field induced by the trapped charge densities, results in a higher order of conduction($\approx 10^{-6}$ h e^{-2}).[51] This higher order of conduction is attributed to an increased charge trap density, causing the formation of additional topological edge states owing to the strong spin Hall effect. The change in charge density
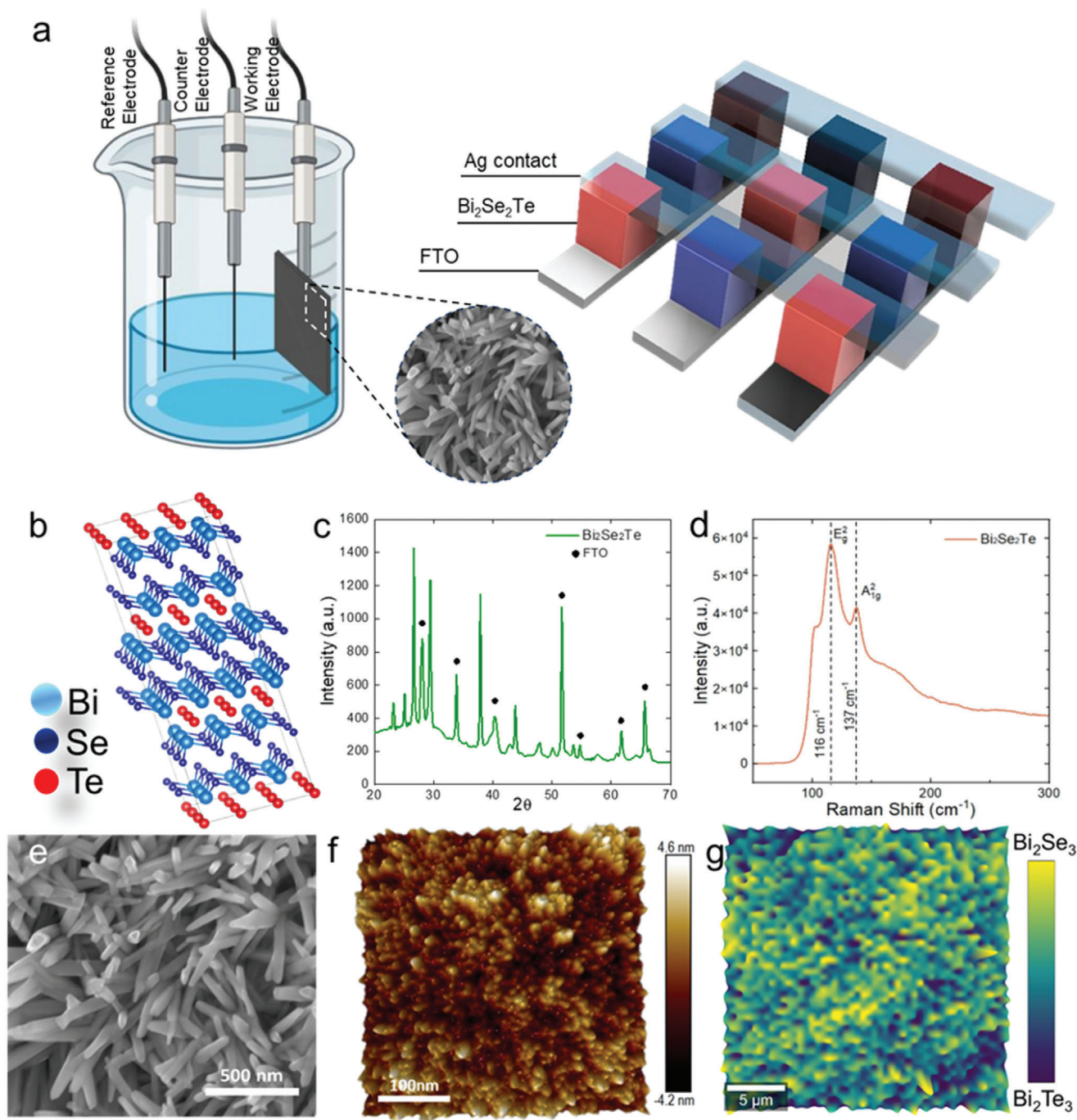
Figure 1. Bismuth selenide telluride material fabrication and characterization. a) Demonstration of the electrochemical deposition (ECD) method to fabricate the synaptic device array. b) Schematic illustration of layered 2D crystal structure of Bi_2Se_2Te. c) X-ray diffraction (XRD) analysis of the prepared thin film demonstrating characteristic peaks of Bi_2Se_2Te. d) Raman scattering plot with characteristic illustration of E_g^2 and A_{1g}^2 peaks. e) Field emission scanning electron microscope (FE-SEM) micrograph exhibiting nanorod structures. f) Atomic force microscope (AFM) roughness topography and g) Raman mapping showing homogenous distribution of the Bi_2Se_2Te thin film.

distribution in the conduction band and the electron localization along the [100] plane at an applied electric field are shown in Figure 2b. The charge distribution and electron localization for Bi_2Se_2Te demonstrate a prominent increase in levels, proving the mechanism of a trap-charge-induced internal electric field.[52]

Following this mechanism, in our developed Bi_2Se_2Te synaptic device, under the influence of an applied voltage stimulus, the trapped charge density increases, thereby inducing an internal electric field to enhance edge state conduction. This leads to ultra-low voltage synaptic switching properties, where
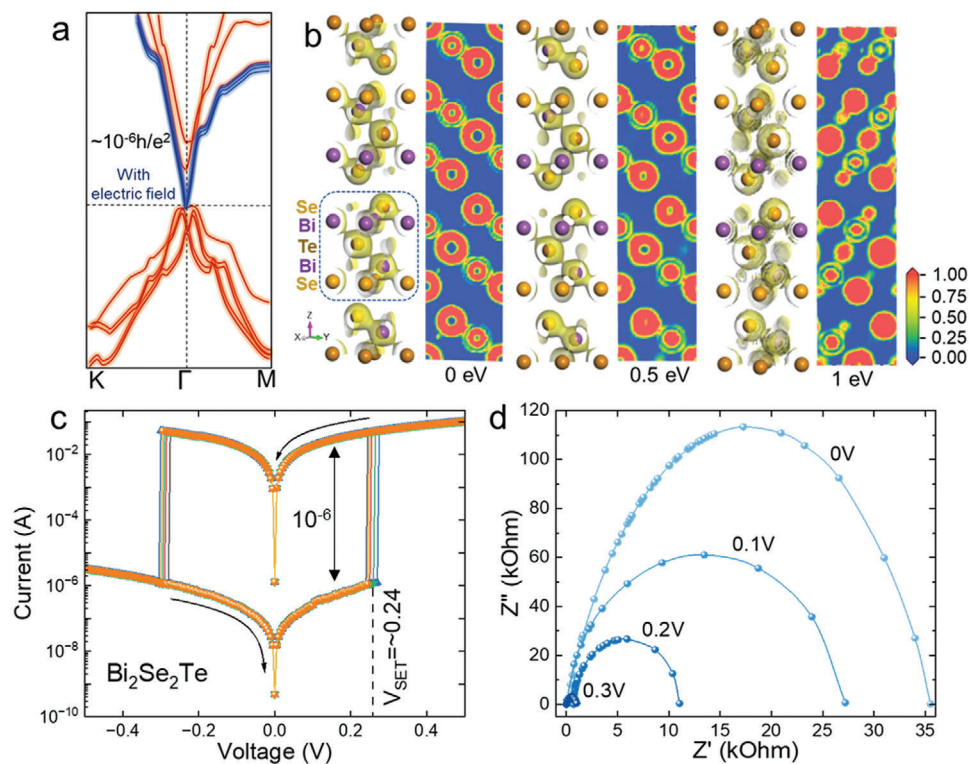
**ADVANCED
SCIENCE NEWS**

www.advancedsciencenews.com

**ADVANCED
MATERIALS**

www.advmat.de

Figure 2. Synaptic device characteristics and quantum switching mechanism. a) Illustrative representation of mechanism involved in topological surface edge state changes induced by an applied electric field. b) Simulation of charge density distribution in conduction band minimum and electron localization function slices of Bi_2Se_2Te under varied electric field in [100] direction. c) Ultra-low threshold $I-V$ switching characteristics of Bi_2Se_2Te. d) Change in impedance state of the synaptic device under applied voltage.

the threshold voltage is set at ≈0.24 V, as seen in Figure 2c; Figures S5–S7, Supporting Information. In addition, to prove the change in the resistance state of the synaptic device, we perform impedance analysis, as shown in Figure 2d. With the increase in the applied voltage stimulus, the impedance level of the device drops significantly. These characteristic results support the development of high-performance, low-power topological neuroelectronic quantum devices. Hence, utilizing the advantageous properties of quantum switching is most favorable for the creation of synaptic devices.[49]

2.2. Quantum Topological Synaptic Device as Neuromodulator

Biologically, neuromodulation in the human brain occurs through the release of event-specific neurotransmitters such as serotonin, dopamine, and acetylcholine. By the principle of Hebbian synaptic plasticity, upon receiving a request at a neuron's presynaptic point, chemical messengers in the form of these neurotransmitters are released from the presynaptic membrane into the synaptic cleft and bind with their corresponding receptors at the postsynaptic membrane. This triggers an action potential as excitatory (EPSP) or inhibitory (IPSP) postsynaptic current to control the synaptic dynamics.[16,17,20] When the membrane potential of the postsynaptic neuron is highly depolarized (+ve), the EPSP is generated with an increase in the firing rate at the postsynaptic neuron, causing a rise in their synaptic weight

through spike-rate dependent plasticity (SRDP). On the contrary, a hyperpolarized (−ve) membrane potential causes a reduction in synaptic weight with respect to the level of IPSP response.[53–56] Thus, the synaptic dynamics are directly modulated by the response level of EPSP and IPSP, causing potentiation or depression between two adjacent neurons or clusters during the neural event.[57–59] However, this biological process of neuromodulation in the human brain deteriorates exponentially with the aging process. Thus, from this understanding of the biological neuromodulation process, it is essential to design a synaptic neuromodulator to potentially defy the cognitive functions that are biologically hindered.

Biomimicking these characteristics of neurotransmitters, in our designed model of a quantum synaptic device, we demonstrate prominent synaptic SRDP behaviors with characteristic EPSP and IPSP responses as a function of applied pulse width modulated presynaptic electric stimuli, which are represented in terms of the stimuli ratio in **Figure 3a**. Here, we define the age-related postsynaptic response to an applied presynaptic stimulus, expressed in terms of the stimuli ratio. For a stimuli ratio larger than 1, it relates to the neural activity of early ages; for a ratio equal to 1, it relates to that of the mid-age range; and for a ratio less than 1, it denotes a decline in the synaptic neural response in elderly individuals. With these presynaptic stimuli ratio classifications, the characteristic behavior of the human brain with respect to the aging process and their corresponding learning efficiency are simulated and represented in Figure 3b.
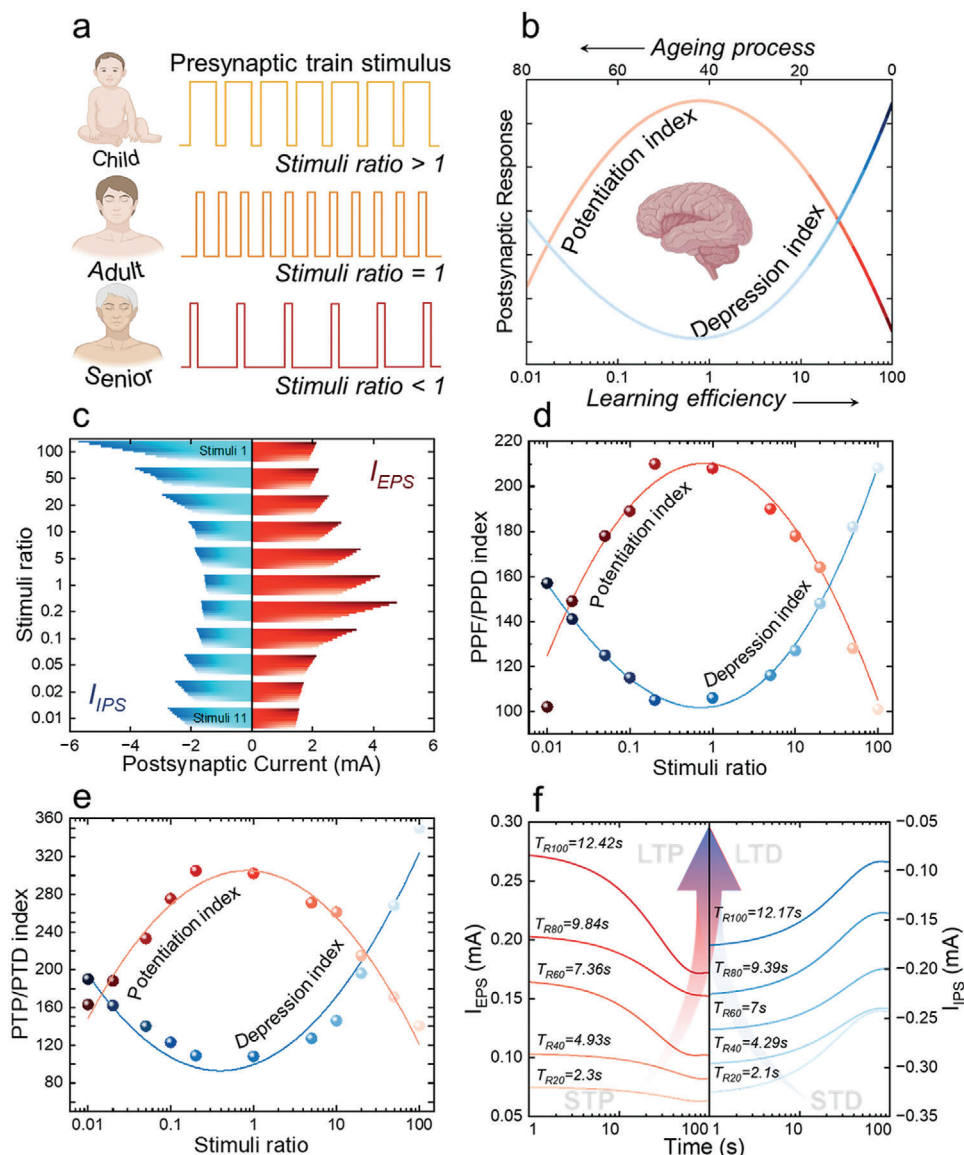
**ADVANCED
SCIENCE NEWS**

www.advancedsciencenews.com

**ADVANCED
MATERIALS**

www.advmat.de

Figure 3. Synaptic neuroelectronic device behavior with ageing-related presynaptic stimuli. a) Schematic illustration of pulse width modulated presynaptic voltage stimuli relating to human brain aging characteristics represented in terms of stimuli ratio. b) Illustrative demonstration of the postsynaptic current response change with ageing process of human brain and their corresponding learning efficiency. c) Experimental postsynaptic current response of I_{EPS} and I_{IPS} for d) their corresponding presynaptic potentiation and depression pulse stimuli trains and e) PPF/PPD and PTP/PTD index change for the varied stimuli ratio. f) Demonstration of synaptic transition from STP to LTP represented in terms of relaxation time.

Emulating these biological characteristics in our device, for an applied presynaptic potentiation pulse stimulus, the I_{EPS} response is prominent only under the conditions of a stimuli ratio equal to 1 representing the brains of mid-age people; whereas, for the early (>1) and old ages (<1), the latency of I_{EPS} is larger as shown in Figure 3c. Conversely, I_{IPS} responses for depressive stimuli are the exact inverse of I_{EPS}. This behavior in our quantum synaptic device is analogous to the biological synaptic response characteristics with respect to different ageing conditions. Moreover, these I_{EPS} and I_{IPS} responses are the important factors accountable for the neuromodulation of synaptic strengths to establish short-term and long-term neural plasticity.[60–62]

Based on the postsynaptic current responses to our presynaptic stimuli, we validate the PPF/PPD indexes, which are the quantification measures of short-term synaptic plasticity efficacies, as shown in Figure 3d.[63] From the inferred PPF and PPD indexes, our results demonstrate a high level of efficacies for the short-term plasticity with respect to their applied stimuli ratios. This PPF/PPD index range indicates the ability of response to establish synaptic strength levels between presynaptic transmitters and postsynaptic receptors. As shown in Figure 3d, in terms of stimuli ratio, the index for potentiation pulse stimuli for mid-age human brain (i.e., stimuli ratio ≈ 1) is at the highest peak, whereas for the early and elderly age individuals' scenario, the ability to respond to establish synaptic

**ADVANCED
SCIENCE NEWS**

www.advancedsciencenews.com

**ADVANCED
MATERIALS**

www.advmat.de

plasticity are under-developed and distorted, respectively. A comparison of PPF indexes for different synaptic devices is shown in Table S2, Supporting Information, which demonstrates the superiority of the Bi_2Se_2Te synaptic device. For the event of presynaptic depression pulse stimuli, the PPD index demonstrates an increasing trend for larger stimuli ratios (>1). Thus, the PPF/PPD index of our synaptic device illustrates the simulation response of short-term neural plasticity characteristics of human brain under age-related conditions. This characteristic behavior in our synaptic device illustrates the capacity to modulate or override the responses owing to ageing or neural disorders in human brain, which can be defined as the process of neuromodulation.

The efficacies of synaptic plasticity strength are associatively quantified via the post-tetanic potentiation/post-tetanic depression index, as illustrated in Figure 3e.[64] As the PPF/PPD efficacies play a crucial role in determining short-term synaptic plasticity, the PTP/PTD index exhibits similar trends, serving as a longer-lasting neural facilitation function in the synaptic device. Equipped with these capabilities, our synaptic device acts as a powerful neuromodulator. We are poised to usher in a new era of brain–computer interfaces, enabling the tuning and repair of age-related damages and neural disorders in the human brain through the control of presynaptic pulse width modulated stimuli.

On the other hand, the ability to retain the short-term or long-term neural plasticity weighted path is a major criterion for a healthy memory system, which governs cognitive functions. Hence, to understand these abilities in our developed synaptic device, we adapt the human brain model proposed by Atkinson and Shiffrin, where the fundamental understanding of memorization events is facilitated through rehearsal learning.[65] The efficacies of the transition from short-term to long-term plasticity in our devices are examined through the estimation of relaxation times for I_{IPS} and I_{EPS} levels, with respect to applied stimuli, as shown in Figure 3f. Our results imply that increasing the applied stimuli from 20 to 100 pulse trains causes exponential enhancements in the relaxation time (T_R), which directly corresponds to the strength of the synaptic weighted path. The relaxation time T_R is calculated by the relation: $I = I_0 + A\exp(-T_R/\tau)$, where A is a constant, I_0 is a current constant, and τ is a relaxation constant.[66] This characteristic increase in synaptic path weight or strength, observed for both potentiation and depression pulse stimuli in our synaptic device, denotes the transition from short-term to long-term neural plasticity. However, this condition applies only to the stimuli ratio of 1 as the relaxation times for older and younger human brains diminish rapidly due to unstable synaptic neural responses.

Though the conversion of the short-term to long-term neural plasticity can be realized via repeated rehearsal learning processes, an increase in the synaptic strength's decay rate leads to loss of memory.[25] Hence, to overcome this phenomenon, in our synaptic device as neuromodulators, irrespective of these stimuli ratio conditions, we demonstrate the tuning of these relaxation times via modulation of the stimuli potential. As shown in **Figure 4a,b**, the decay rate (% s^{-1}) of these synaptic strengths increases with respect to the increase in the stimuli potential in both the cases of potentiation/depression presynaptic stimuli.

This demonstration of a decrease in the decay rate proves the ability to induce anti-ageing phenomenon in our design of quantum synaptic neuromodulators. These properties are achieved via an edge state trapped-charged mechanism, where more charges are being accumulated/consumed in the developed additional topological edge states; while, applying potentiation/depression stimuli. As seen in Figure 4a,b, when applying the potentiation/depression stimuli, the auto-depression behavior decreases due to the intensification of the charged-trapping effect, which enhances the synaptic path weightage or strength.[1,25,67] The observed declining decay rates for the respective response of the I_{EPS} and I_{IPS} levels are represented in Figure 4c. Thus, with an optimum voltage level, reversal of the ageing process in human brain can be accomplished via neuromodulating the decay rate of the synaptic strengths.

However, as PPF indexes are a preliminary factor for modulating synaptic strength from short-term to long-term, we aim to correlate changes in the PPF index with changes in amplitude-modulated synaptic pulse stimuli. To do this, we analyze electric field-dependent paired-pulse facilitation characteristics. The level of trapped charges in the Bi_2Se_2Te layers enhances the electric field, which directly corresponds to an increase in synaptic strength, thereby decreasing the decay rate in our synaptic neuromodulator device. An increase in the internal electric field, owing to the trapped charge density in the Bi_2Se_2Te thin films, leads to variations in the topological band structure, which can be expressed as:

$$n = \frac{1}{3\pi^2 h^3} \left(\frac{2m^* e^2}{4\pi\varepsilon\varepsilon_0} \right)^{3/2} N_T^{1/2} \tag{1}$$

where, m^* is the effective mass of the charge carrier and N_T is the charge trap density.[47] The change in the carrier concentration and the effective mass with respect to the selenium ratios is shown in Figure S4, Supporting Information.

In the human brain, the magnitude of the PPF function is directly related to the age factor. As people age, the synaptic PPF index theoretically shows a consistent decrease in neural activities, leading to a gradual loss of communication strength between neighboring neurons. For elderly individuals, slower stimulus trains lead to a reduction in synaptic weight, which negatively affects the efficiency of learning activities. In contrast, young individuals achieve higher learning efficiency with a faster stimulus train rate.[1,25] With similar characteristics, our synaptic neuromodulator device successfully bio-mimics the human neural network's learning activity for both elderly and young individuals. The EF-PPF properties of the synapse, as demonstrated in Figure 4d, are determined via the slope index (I_S), which quantifies the PPF index according to the relation PPF = $(\Delta t)^{(I_S/100)}$. It can be observed that with potentiation stimuli, I_S index increases; while, applying a higher negative-positive bias. This is contrary to the negative I_s index, which gradually decreases in parallel with higher positive voltage bias (Figure S13, Supporting Information). This flexibility in EF-PPF demonstrates a direct correlation between the interval of rehearsal events and learning efficiency under various voltage biases, showcasing the device's excellent ability to mimic the neural plasticity of the human brain. Thus, by decreasing the decay rate or increasing synaptic
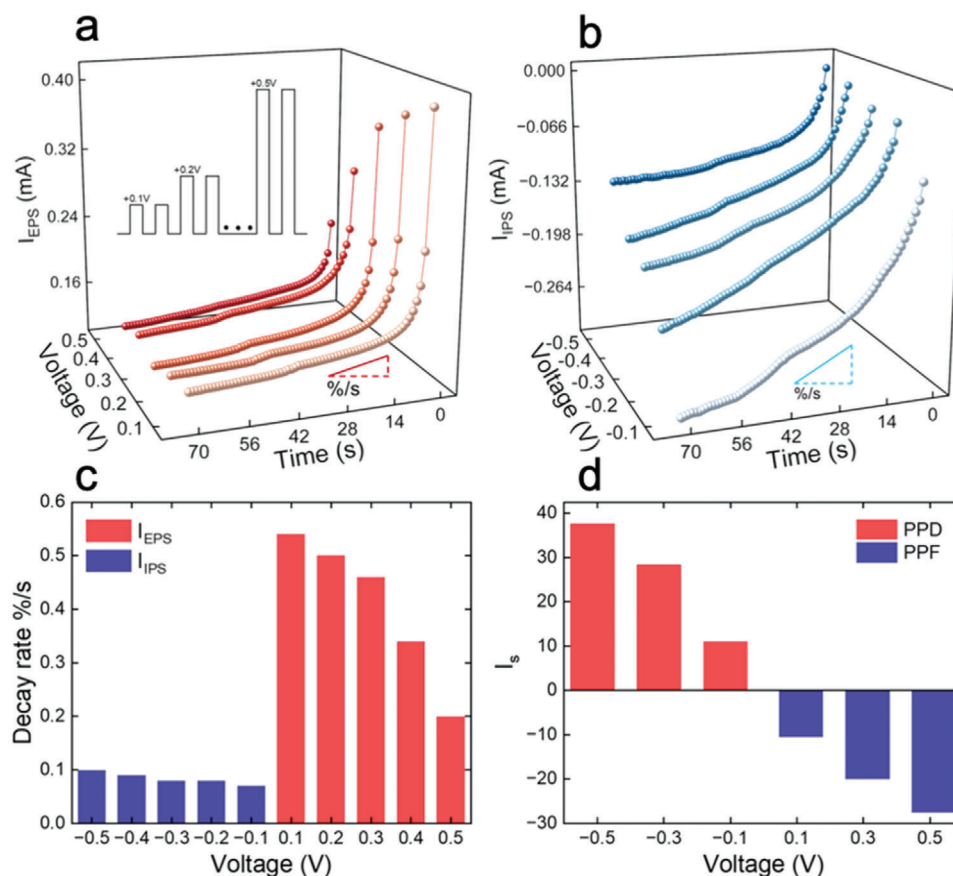
2306254 (6 of 12)

**ADVANCED
SCIENCE NEWS**

www.advancedsciencenews.com

**ADVANCED
MATERIALS**

www.advmat.de

Figure 4. Pulse amplitude modulated synaptic strength tuning in Bi_2Se_2Te synaptic device. a) Excitatory post-synaptic current relaxation time (decay rate) for different pulse amplitude range from 0.1 to 0.5 V. b) Inhibitory post-synaptic current relaxation time (decay rate) for different pulse amplitude range from −0.1 to −0.5 V. c) Auto-depression decay rate for pulse amplitude modulated presynaptic stimuli. d) Correlation of electric field-dependent PPF characteristics (EF-PPF) for the change in synaptic strength which is calculated based on slope index levels.

strength via amplitude-modulated presynaptic pulse stimuli, we can achieve faster learning and enhance memory longevity in the human brain.

2.3. Real-Time Neuromodulation of EEG for Brain–Computer Interface

As a proof of concept, we demonstrate the neuromodulation of aging-distorted ERP signals deduced from EEG signals of a group of elderly individuals collected during auditory-cued reaction time tasks. ERPs are the measure of voltage change in the human brain followed by visual, auditory, or sensory stimuli.[68] As illustrated in **Figure 5a**, characteristic ERP components are represented with P1/N1 in the region of 100 ms, N2 region around 200–300 ms, P3 region between 300 and 500 ms, and N4 region between 400 and 600 ms. These characteristic components represent sensory stimuli processing (P1/N1), attentional monitoring (N2), memory and decision-making processes (P3), and semantic processing (N4), respectively.[68] From deduced ERPs, we can understand the neural activities to assess the brain's functional health levels in persons affected by aging-related and Alzheimer's or Parkinson's diseases.[69]

From previous reports, it is well observed that, with respect to brain aging, the levels of attenuation in P3 and N4 components are seriously distorted, causing major cognitive dysfunctions.[69] Thus, modulating the ERPs with an effective modulation index is of utmost importance for brain–computer interfaces in assisting applications such as neuroprosthetics, epilepsy management, and treating memory impairments in elderly individuals. Following this, we demonstrate real-time neuromodulation of distorted ERPs to establish bidirectional communication as a brain–machine interface.

Figure 5a demonstrates the mechanism of the neuromodulation process through the steps of EEG acquisition and processing, ERP component extraction, ERP-PWM encoding, neuromodulation, and feedback. For the real-time study, we collect EEG datasets from individuals of different age groups, from which we extract the ERPs, as shown in Figure 5b. In our analysis, we interpret an auditory cue reaction time tasks dataset of 39 ERPs belonging to elderly individuals aged in the range of 55–75 years and a reference ERP from a young individual. The raw ERPs obtained from elderly individuals illustrate an increase in the distortion of P3 and N4 components compared to the reference signal, as shown in Figure 5c. However, the process of modulating a neural signal requires intelligent event-specific
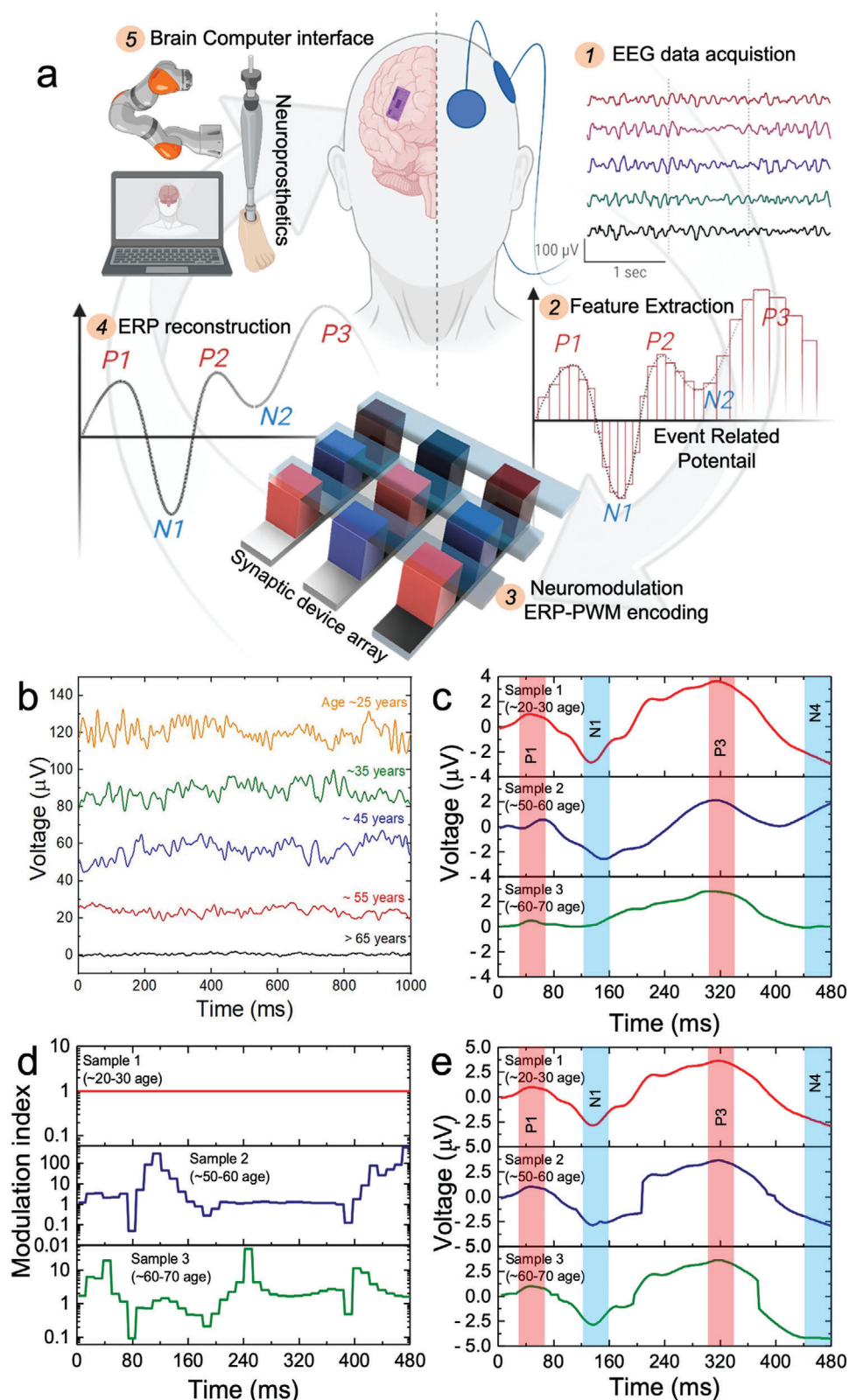
Figure 5. Real-time modulation of EEG–ERPs neural signals. a) Step-by-step illustration of neuromodulation process involving i) EEG data acquisition, ii) ERPs feature extraction and signal sampling, iii) neuromodulation process using synaptic device, iv) signal reconstruction, and v) brain computer interfacing as neuroprosthetic controls. b) EEG dataset from different age groups of people. c) Extracted ERPs. d) modulation index derived from changing resistance state of synaptic device. e) Reconstructed boosted ERPs for BCI.

2306254 (8 of 12)

**ADVANCED
SCIENCE NEWS**

www.advancedsciencenews.com

**ADVANCED
MATERIALS**

www.advmat.de

signal modulation, which can only be performed through the training of neuromorphic synaptic devices. In this case, the modulation index or factor is obtained from the ratio of the change in conductance to the reference conductance in our synaptic device array, as shown in Figure 5d.

To obtain the modulation index, the raw ERP dataset is processed into pulse width modulated signals via sampling, similar to the illustration in Figure 2a, which is then applied as pulse stimuli to the synaptic device. Further, the neuromodulated signals are developed using the modulation index together with the real dataset to make them recognizable without additional resources. This modulation boosts ERPs to similar strengths as the reference ERPs for every representative peak component, as shown in Figure 5e. From this process, neuromodulated ERPs for any specific task can be obtained for brain–computer interface applications.

3. Conclusion

Our developed synaptic neuroelectronic device utilizes the unique properties of the Bi_2Se_2Te QTI, marking a significant advancement in neuromorphic technologies for brain–computer interfaced neuroprosthetics. The demonstrated synaptic neuroelectronic device addresses critical aspects of power consumption (picojoules), data switching/processing speed (ms), and neuromorphic learning efficiency. These high-class properties arise from the electronic surface states' transport characteristics of Bi_2Se_2Te to achieve synchronous synaptic switching and a flexible PPF/PPD neuromodulation index that closely resembles the dynamics of biological neurons. This flexible neuromodulation behavior in a neuroelectronic device is being reported for the first time, offering precise control capacity in the learning-to-forget process of the human brain to shape their electrophysiological activities. To evaluate the neuromodulation performance of our synaptic neuroelectronic device, we demonstrate real-time neuromodulation of EEG derived ERPs of elderly individuals with cognitive dysfunctions to match the healthy neural function of young individuals for brain–computer interface applications. Our results prove the possibility of controlled synchronization and memory function longevity in human brain performance, thereby mitigating the causes and impacts of aging and neurological disorders in human life.

4. Experimental Section

Fabrication of the Synaptic Neuroelectronic Device: Topological insulators-based thin films (Bi_2Se_3, Bi_2Te_3, and Bi_2Se_2Te) were meticulously fabricated on the fluorine-doped tin oxide (FTO) glass substrate, which imitated the postsynaptic neuron behavior. The functional/active layer of the synaptic device was deposited utilizing the three-electrode ECD technique. The emulation of presynaptic neurons was achieved through the utilization of a top electrode (100 nm), fabricated using a thermal evaporation technique. Before the deposition, the FTO-coated glass substrates underwent a cleaning process involving sequential immersions in DI water, acetone, and ethanol for a duration of 30 min within an ultrasonic bath. The fabrication of the Bi_2Se_3, Bi_2Te_3, and Bi_2Se_2Te active layers was accomplished through the implementation of the ECD method, which was conducted using the Metrohm Autolab PGSTAT302 instrument. To ensure precise monitoring and control of the electrochemical potential throughout the fabrication process, the Ag/AgCl

double junction reference electrode and high-purity platinum counter electrode were employed. A FTO-coated glass substrate (exposed area of $1 cm^2$ and sheet resistance of $\approx 7\ ohm\ sq^{-1}$) played the role of working electrode. Throughout each deposition, the distance between the anode and cathode remained fixed at 0.5 cm. The deposition bath comprised 50 mL of deionized water (>18 Mohm), sourced from a Purite (L300450) system. First, 2.08 mL of HNO_3 was added to the DI solution, resulting in pH < 1. Second, under stirring, 0.485 g of $BiNO_3*5H_2O$ was added to the solution. Subsequently, the solution underwent sonication for a duration of a 10 min, continuing until it achieved complete transparency. Third, stirring of the 0.166 g of the SeO_2 and 0.08 g of the TeO_2 was followed by 10 min sonication process. Then, the mixture was subjected to a gentle purge with purified nitrogen gas for a duration of 60 min. This process effectively eliminated any dissolved oxygen present in the solution. During the deposition process, the bath temperature was consistently maintained at 60 °C. After the deposition, the samples were gently washed with deionized water and subsequently annealed in a nitrogen atmosphere at 300 °C for a duration of 3 h. The fabricated thin films exhibited a uniform appearance and excellent adhesion to the FTO substrate.

Material Characterization of the Synaptic Device: The surface morphology of the Bi_2Se_3, Bi_2Te_3, and Bi_2Se_2Te thin films was examined and verified using the Hitachi SU8240 field emission scanning electron microscope (FE-SEM). The structural characteristics of the fabricated thin films were confirmed through the utilization of powder X-ray diffraction (XRD) Rigaku Miniflex diffractometer. The surface roughness was confirmed using the Bruker Dimension HPI atomic force microscope (AFM) with a scan rate of 0.996 Hz. The Raman properties were validated by the Horiba Labram HR Raman System, employing a 532 nm laser. The measurement of carrier density and mobility were performed at room temperature using the Lakeshore Hall measurement system.

Synaptic Switching and Neuromorphic Characterization of the Device: The electrical characterization and switching properties of the developed synaptic neuromodulator device were performed utilizing a probe station that was equipped with the Agilent Technologies B1500A Semiconductor Device Analyzer. The digital storage oscilloscope was used for the data acquisition process. Synaptic switching properties were examined and verified by applying the sequential sweep voltages to the synaptic device to obtain $I–V$ characteristics. SRDP was investigated by applying a series of ten consecutive pulse stimuli to the presynaptic neuron. The stimulus pattern was characterized in relation to the stimuli ratio, represented as a function of the pulse width. The pulse amplitude was fixed at +100mV/−100mV throughout the measurement. The resulting inhibitory postsynaptic current (I_{IPC}) and excitatory postsynaptic current (I_{EPC}) responses were measured and subjected to comprehensive analysis. PPF/PPD was deeply analyzed by applying two consecutive pulse stimuli to the presynaptic neuron with relation to the stimuli ratio, represented as a function of the pulse width. The pulse amplitude was fixed at +100mV/−100mV throughout the measurement. By evaluating the postsynaptic current response to the predefined stimuli, the PPF/PPD index was calculated, providing a quantitative representation of short-term synaptic plasticity. The PPF/PPD index was determined using the following formula PPF/PPD index = A_2/A_1, where A1 and A2 represent the post-synaptic current responses elicited by the first and second pulses, respectively. Post-tetanic potentiation (PTP)/post-tetanic depression (PTD) was investigated by applying ten consecutive pulse stimuli with a predefine stimuli ratio (as a function of the pulse width) to the presynaptic neuron. The pulse amplitude was fixed at +100mV/−100mV throughout the measurement. Through the evaluation of the postsynaptic current response to the applied stimuli, the PTP/PTD index was calculated, serving as a quantitative measure of short-term synaptic plasticity. The PPF/PPD index was determined using the following formula PTP/PTD index = A_{10}/A_1, where A_1 and A_{10} represent the post-synaptic current responses elicited by the first and second pulses, respectively. The transition process from short-term potentiation/depression (STP/STD) to long-term potentiation/depression (LTP/LTD) was examined and verified by applying a sequence of the consecutive presynaptic pulse stimuli, consisting of 20, 40, 60, 80, and 100 pulses. The pulse amplitude was fixed at +100
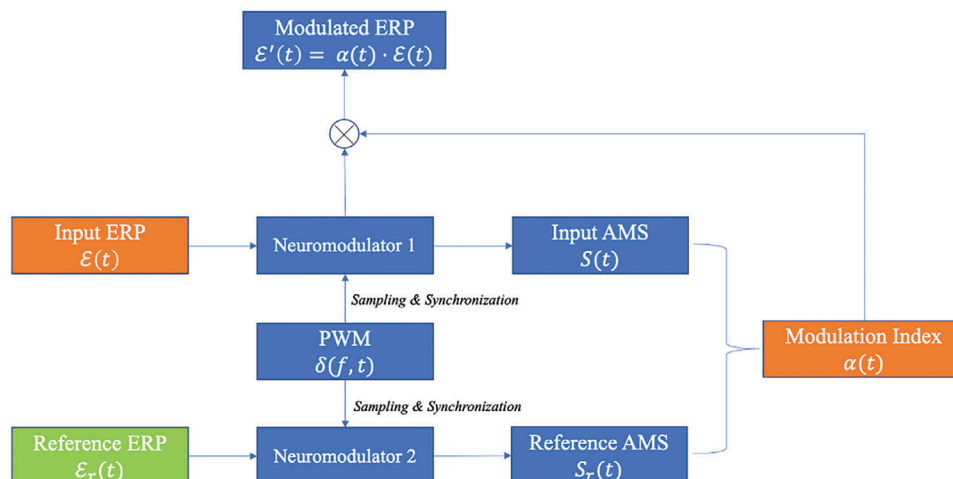
**ADVANCED
SCIENCE NEWS**

www.advancedsciencenews.com

**ADVANCED
MATERIALS**

www.advmat.de

Figure 6. Mathematical modeling of the neuromodulation process.

mV/−100 mV throughout the measurement. The obtained results were subjected to fitting and analysis using an exponential equation that was commonly utilized as a forgetting function in psychology. The formula, expressed as ($I = I_0 + A \times e^{[-t/\tau]}$) was employed, where A represents a constant amplitude, I_0 represents a constant current, and τ measures the relaxation constant, reflecting the rate of decay, which is the value of interest. Synaptic strength tuning (auto-depression rate) characteristic of the synaptic device was directly influenced by the temporal evolution of synaptic strength, a parameter intricately connected to age-related neuroplastic changes within the brain. This property was investigated through the application of five groups, each comprising 20 consecutive pulse stimuli to the presynaptic neuron. The stimuli were administered with a fixed pulse interval of 100 ms, a pulse width of 100 ms, and a pulse amplitude range from −0.1/0.1V to −0.5/0.5V. The time-dependent synaptic plasticity was examined, and the auto-depression rate was measured and extracted at intervals of 70 s. The comprehensive statistical analysis of 50 devices further corroborates the trends described above. The minimal variation observed between devices could be attributed to the uniformity of the thin films fabricated via the electrochemical deposition technique. Contrary to conventional inorganic, organic, and oxide-based devices, the authors' topological insulator-based devices exhibited exceptional synaptic switching performance of ≈10⁻⁶ s and a remarkably low energy consumption level of ≈17 pJ (Figures S8 and S9 and Tables S1 and S3, Supporting information).

Neuromodulation of Aging Distorted ERP Signals Deduced From EEG Signals: The authors' study did not involve direct experimentation with human participants or tissue samples. Instead, publicly available datasets were utilized from OpenNeuro (https://openneuro.org, license: CC0).[70] Therefore, the requirements for ethics committee approval and informed consent for the authors' analysis were not applicable. For the author experiment, an EEG dataset associated with auditory cue reaction time tasks was selected, from which the authors subsequently derived further ERP signals. Out of the 39 elderly individuals, aged between 55 and 75 years, five distinctive ERPs were selected for further in-depth analysis. As a reference point, a sample consisting of a young individual demonstrating optimal brain function was selected. 64 channels of EEG signals with an acquisition rate of 500 Hz were provided in the dataset. From all the channels, FCz electrode was selected for ERPs analysis as it was located over the mid-front cortex of the brain, which reflected the cognitive processes. The raw EEG signals for each person were filtered by a band-pass filter with cutoff frequencies of 0.1–30 Hz, after which, ICA (independent component analysis) was applied to remove the artifacts from eyes and muscles. The pre-processed EEG signals for individuals were then segmented by the onset of the event and the event-related parts of the EEG signals were averaged to calculate the ERPs. After that, the ERPs were sampled every 12 ms to get event-related pulses as the inputs of the authors' de-

vice for further modulation. The above experiment protocol and method of real-time modulation of EEG-ERP neural signals made them highly reproducible.

Mathematical modeling of the neuromodulation is shown in **Figure 6** and was expressed as:

Assuming that the authors' device was working on a fundamental frequency f and the ERP that was received over time was $\mathcal{E}(t)$, the procedure of ERP modulation based on a reference ERP, $\mathcal{E}_r(t)$, was illustrated in the following steps:

To begin with, the ERP $\mathcal{E}(t)$ was converted into an amplitude-modulated square wave (AMS) signal $S(t)$ which was expressed as:

$$S(t) = \mathcal{E}(t) \times \delta(f, t) \tag{2}$$

where $\delta(f, t)$ was a PWM function operating at frequency f, producing output values of 1 or 0 in each cycle.

Likewise, the AMS of reference ERP was expressed as $S_r(t) = \mathcal{E}_r(t) \times \delta(f, t)$, in which the PWM function was identical to the one used in $S(t)$, enabling the alignment of $S(t)$ and $S_r(t)$. Further, the modulation index $\alpha(t)$, which presents how much the received ERP should be modulated to fit with the reference ERP, was calculated by the AMS as:

$$\alpha(t) = \begin{cases} \frac{|S_r(t)|}{|S(t)|}, & \text{if } t \in t_{on} \\ \alpha(t-1), & \text{if } t \in t_{off} \end{cases} \tag{3}$$

where t_{on} and t_{off} were the on and off periods of the PWM $\delta(f, t)$. After that, $\alpha(t)$ was applied back to the original ERP received by the authors' device to obtain the modulated ERP $\mathcal{E}'(t) = \alpha(t) \times \mathcal{E}(t)$. The whole procedure of the modulation was expressed as below:

$$\mathcal{E}'(t) = \frac{|\mathcal{E}_r(t) \times \delta(f, t)|}{|\mathcal{E}(t) \times \delta(f, t)|} \times \mathcal{E}(t) \times [t \in t_{on}]$$

$$+ \frac{|\mathcal{E}_r(t-1) \times \delta(f, t-1)|}{|\mathcal{E}(t-1) \times \delta(f, t-1)|} \times \mathcal{E}(t) \times [t \in t_{off}] \tag{4}$$

where $[t \in t_{on}]$ and $[t \in t_{off}]$ were the indicator functions that took the value of 1 when the condition held true and the value of 0 when it was false.

Statistical Analysis: A statistical analysis was performed on 50 devices for each topological insulator material (Bi_2Se_3, Bi_2Se_2Te, and Bi_2Te_3) using Origin and MATLAB software for processing and analysis. The standard deviation for the data was observed to be within ±5%. To ensure comparability and enhance interpretability across different samples, max

**ADVANCED
SCIENCE NEWS**

www.advancedsciencenews.com

**ADVANCED
MATERIALS**

www.advmat.de

normalization was applied to scale the data. Subsequently, a *t*-test was utilized to evaluate the significance of differences between groups, resulting in a *p*-value < 0.05.

Supporting Information

Supporting Information is available from the Wiley Online Library or from the author.

Conflict of Interest

The authors declare no conflict of interest.

Author Contributions

D.S.A. and V.K. contributed to conceptualization, methodology, visualization, formal analysis, and writing-original draft. H.H. and V.C.S.T. contributed to software, resources, and data curation. M.M.d.S. contributed to validation, investigation, writing-review and editing. V.A.L.R. contributed to conceptualization, supervision, funding acquisition, project administration, and writing-review and editing.

Data Availability Statement

The data that support the findings of this study are available from the corresponding author upon reasonable request.

[1] S. J. Moore, G. G. Murphy, in *Handbook of the Biology of Aging*, 8th ed. (Eds: N. Musi, P. Hornsby), Elsevier, Amsterdam, the Netherlands **2016**, pp. 391–405.

[2] T. J. Park, S. Deng, S. Manna, A. N. M. N. Islam, H. Yu, Y. Yuan, D. D. Fong, A. A. Chubykin, A. Sengupta, S. K. R. S. Sankaranarayanan, S. Ramanathan, *Adv. Mater.* **2023**, *35*, 2203352.

[3] N. Ilyas, J. Wang, C. Li, D. Li, H. Fu, D. Gu, X. Jiang, F. Liu, Y. Jiang, W. Li, *Adv. Funct. Mater.* **2022**, *32*, 2110976.

[4] F. Torres, A. C. Basaran, I. K. Schuller, *Adv. Mater.* **2023**, *35*, 2205098.

[5] Y. Sun, Y. Ding, D. Xie, *Adv. Funct. Mater.* **2021**, *31*, 2105625.

[6] J. Robinnharris, V. Korolchuk, *Springer Nature* **2019**, 91.

[7] S. Ballesteros, L. G. Nilsson, P. Lemaire, *Eur. J. Cogn. Psychol.* **2009**, *21*, 161.

[8] D. C. Park, T. A. Polk, J. A. Mikels, S. F. Taylor, C. Marshuetz, *Dialogues Clin. Neurosci.* **2001**, *3*, 151.

[9] N. Dennis, J. Koen, *Aging, Neuropsychol., Cogn.* **2022**, *29*, 367.

[10] D. C. Park, G. N. Bischof, *Dialogues Clin. Neurosci.* **2013**, *15*, 109.

[11] X. Tang, P. Huang, Y. Li, J. Lan, Z. Yang, M. Xu, W. Yi, L. Lu, L. Wang, N. Xu, *Front. Cell Neurosci.* **2019**, *13*, 469.

[12] X. Chen, B. Chen, B. Jiang, T. Gao, G. Shang, S.-T. Han, C.-C. Kuo, V. A. L. Roy, Y. Zhou, *Adv. Funct. Mater.* **2023**, *33*, 2208807.

[13] H. Liu, Y. Qin, H. Chen, J. Wu, J. Ma, Z. Du, N. Wang, J. Zou, S. Lin, X. Zhang, Y. Zhang, H. Wang, *Adv. Mater.* **2023**, *35*, 2205047.

[14] C. López, *Adv. Mater.* **2023**, *35*, 2208683.

[15] D. Hao, Z. Yang, J. Huang, F. Shan, *Adv. Funct. Mater.* **2023**, *33*, 2211467.

[16] X. Wang, Y. Zong, D. Liu, J. Yang, Z. Wei, *Adv. Funct. Mater.* **2023**, *33*, 2213894.

[17] G. Lee, J.-H. Baek, F. Ren, S. J. Pearton, G.-H. Lee, J. Kim, *Small* **2021**, *17*, 2100640.

[18] X. Wang, H. Yang, E. Li, C. Cao, W. Zheng, H. Chen, W. Li, *Small* **2023**, *19*, 2205395.

[19] H. Liu, D. Liu, J. Yang, H. Gao, Y. Wu, *Small* **2023**, *19*, 2206938.

[20] H. Bian, Y. Y. Goh, Y. Liu, H. Ling, L. Xie, X. Liu, *Adv. Mater.* **2021**, *33*, 2006469.

[21] C. Han, X. Han, J. Han, M. He, S. Peng, C. Zhang, X. Liu, J. Gou, J. Wang, *Adv. Funct. Mater.* **2022**, *32*, 2113053.

[22] S. Ling, C. Zhang, C. Ma, Y. Li, Q. Zhang, *Adv. Funct. Mater.* **2023**, *33*, 2208320.

[23] L. Zhou, S. Yang, G. Ding, J.-Q. Yang, Y. Ren, S.-R. Zhang, J.-Y. Mao, Y. Yang, Y. Zhou, S.-T. Han, *Nano Energy* **2019**, *58*, 293.

[24] J.-H. Wang, P. T. Kelly, *J. Neurophysiol.* **1997**, *78*, 2707.

[25] K.-C. Lee, M. Li, Y.-H. Chang, S.-H. Yang, C.-Y. Lin, Y.-M. Chang, F.-S. Yang, K. Watanabe, T. Taniguchi, C.-H. Ho, C.-H. Lien, S.-P. Lin, P.-W. Chiu, Y.-F. Lin, *Nano Energy* **2020**, *77*, 105258.

[26] Y. Temel, A. Jahanshahi, *Science* **2015**, *347*, 1418.

[27] A. M. Lozano, N. Lipsman, H. Bergman, P. Brown, S. Chabardes, J. W. Chang, K. Matthews, C. C. McIntyre, T. E. Schlaepfer, M. Schulder, Y. Temel, J. Volkmann, J. K. Krauss, *Nat. Rev. Neurol.* **2019**, *15*, 148.

[28] S. M. Won, E. Song, J. T. Reeder, J. A. Rogers, *Cell* **2020**, *181*, 115.

[29] R. Chen, A. Canales, P. Anikeeva, *Nat. Rev. Mater.* **2017**, *2*, 16093.

[30] M. L. Kringelbach, N. Jenkinson, S. L. F. Owen, T. Z. Aziz, *Nat. Rev. Neurosci.* **2007**, *8*, 623.

[31] F. Lotti, F. Ranieri, G. Vadalà, L. Zollo, G. Di Pino, *Front. Neurosci.* **2017**, *11*, 497.

[32] A. Sridharan, S. D. Rajan, J. Muthuswamy, *J. Neural Eng.* **2013**, *10*, 066001.

[33] S. Luan, I. Williams, K. Nikolic, T. G. Constandinou, *Front. Neuroeng.* **2014**, *7*, https://doi.org/10.3389/fneng.2014.00027.

[34] K. Deisseroth, *Nat. Methods* **2011**, *8*, 26.

[35] E. S. Boyden, F. Zhang, E. Bamberg, G. Nagel, K. Deisseroth, *Nat. Neurosci.* **2005**, *8*, 1263.

[36] G. Hong, A. L. Antaris, H. Dai, *Nat. Biomed. Eng.* **2017**, *1*, 0010.

[37] X. Yang, E. McGlynn, R. Das, S. P. Paşca, B. Cui, H. Heidari, *Adv. Mater.* **2021**, *33*, 2103208.

[38] Y.-S. Huang, C.-H. Fan, N. Hsu, N.-H. Chiu, C.-Y. Wu, C.-Y. Chang, B.-H. Wu, S.-R. Hong, Y.-C. Chang, A. Yan-Tang Wu, V. Guo, Y.-C. Chiang, W.-C. Hsu, L. Chen, C. Pin-Kuang Lai, C.-K. Yeh, Y.-C. Lin, *Nano Lett.* **2020**, *20*, 1089.

[39] M. Hallett, *Nature* **2000**, *406*, 147.

[40] M. Lu, S. Ueno, *PLoS One* **2017**, *12*, e0178422.

[41] S. Bhattacharyya, G. Akhgar, M. Gebert, J. Karel, M. T. Edmonds, M. S. Fuhrer, *Adv. Mater.* **2021**, *33*, 2007795.

[42] X. Zhang, Y. Zhang, H. Yu, H. Zhao, Z. Cao, Z. Zhang, Y. Zhang, *Adv. Mater.* **2023**, *35*, 2207966.

[43] I. D. Bernardo, J. Hellerstedt, C. Liu, G. Akhgar, W. Wu, S. A. Yang, D. Culcer, S.-K. Mo, S. Adam, M. T. Edmonds, M. S. Fuhrer, *Adv. Mater.* **2021**, *33*, 2005897.

[44] Y. Xu, Y. R. Chen, J. Wang, J. F. Liu, Z. Ma, *Phys. Rev. Lett.* **2019**, *123*, 206801.

**ADVANCED
SCIENCE NEWS**

www.advancedsciencenews.com

**ADVANCED
MATERIALS**

www.advmat.de

[45] M. Nadeem, C. Zhang, D. Culcer, A. R. Hamilton, M. S. Fuhrer, X. Wang, *Appl. Phys. Rev.* **2022**, *9*, 011411.

[46] D. Wang, Z. Wang, N. Xu, L. Liu, H. Lin, X. Zhao, S. Jiang, W. Lin, N. Gao, M. Liu, G. Xing, *Adv. Sci.* **2022**, *9*, 2203006.

[47] S. A. Iyengar, A. B. Puthirath, V. Swaminathan, *Adv. Mater.* **2022**, *35*, 2107839.

[48] S. Izadi, A. Bhattacharya, S. Salloum, J. W. Han, L. Schnatmann, U. Wolff, N. Perez, G. Bendt, I. Ennen, A. Hütten, K. Nielsch, S. Schulz, M. Mittendorff, G. Schierning, *Small* **2023**, *19*, 2204850.

[49] D. S. Assi, H. Huang, V. Karthikeyan, V. C. S. Theja, M. M. de Souza, N. Xi, W. J. Li, V. A. L. Roy, *Adv. Sci.* **2023**, *10*, 2300791.

[50] M. J. Gilbert, *Commun. Phys.* **2021**, *4*, 70.

[51] S. Shekhar, Y. Oh, J.-Y. Jeong, Y. Choi, D. Cho, S. Hong, *Mater. Horiz.* **2023**, *10*, 2245.

[52] Y. Ruan, L. Huang, Y. Yang, G. Xu, K. Zhong, Z. Huang, J.-M. Zhang, *Phys. Chem. Chem. Phys.* **2020**, *22*, 3867.

[53] Y. Wang, Y. Zhu, Y. Li, Y. Zhang, D. Yang, X. Pi, *Adv. Funct. Mater.* **2022**, *32*, 2107973.

[54] J. Zhu, T. Zhang, Y. Yang, R. Huang, *Appl. Phys. Rev.* **2020**, *7*, 011312.

[55] Y. He, Y. Yang, S. Nie, R. Liu, Q. Wan, *J. Mater. Chem. C* **2018**, *6*, 5336.

[56] M. M. Mburu, K.-T. Lu, N. L. Prine, A.-N. Au-Duong, W.-H. Chiang, X. Gu, Y.-C. Chiu, *Adv. Mater. Technol.* **2022**, *7*, 2101506.

[57] J. Tang, C. He, J. Tang, K. Yue, Q. Zhang, Y. Liu, Q. Wang, S. Wang, N. Li, C. Shen, Y. Zhao, J. Liu, J. Yuan, Z. Wei, J. Li, K. Watanabe, T. Taniguchi, D. Shang, S. Wang, W. Yang, R. Yang, D. Shi, G. Zhang, *Adv. Funct. Mater.* **2021**, *31*, 2011083.

[58] J.-Y. Mao, L. Hu, S.-R. Zhang, Y. Ren, J.-Q. Yang, L. Zhou, Y.-J. Zeng, Y. Zhou, S.-T. Han, *J. Mater. Chem. C* **2019**, *7*, 48.

[59] F. Sun, Q. Lu, L. Liu, L. Li, Y. Wang, M. Hao, Z. Cao, Z. Wang, S. Wang, T. Li, T. Zhang, *Adv. Mater. Technol.* **2020**, *5*, 1900888.

[60] H.-K. He, R. Yang, W. Zhou, H.-M. Huang, J. Xiong, L. Gan, T.-Y. Zhai, X. Guo, *Small* **2018**, *14*, 1800079.

[61] F. Nadim, D. Bucher, *Curr. Opin. Neurobiol.* **2014**, *29*, 48.

[62] D. Bucher, E. Marder, *Cell* **2013**, *155*, 482.

[63] J. Shi, J. Jie, W. Deng, G. Luo, X. Fang, Y. Xiao, Y. Zhang, X. Zhang, X. Zhang, *Adv. Mater.* **2022**, *34*, 2200380.

[64] Y. Chen, Y. Kang, H. Hao, X. Xie, J. Zeng, T. Xu, C. Li, Y. Tan, L. Fang, *Adv. Funct. Mater.* **2023**, *33*, 2209781.

[65] R. M. Shiffrin, R. C. Atkinson, *Psychol. Rev.* **1969**, *76*, 179.

[66] H.-L. Park, Y. Lee, N. Kim, D.-G. Seo, G.-T. Go, T.-W. Lee, *Adv. Mater.* **2020**, *32*, 1903558.

[67] P. Moretti, J. M. Levenson, F. Battaglia, R. Atkinson, R. Teague, B. Antalffy, D. Armstrong, O. Arancio, J. D. Sweatt, H. Y. Zoghbi, *J. Neurosci.* **2006**, *26*, 319.

[68] J. Kropotov, V. Ponomarev, E. P. Tereshchenko, A. Müller, L. Jäncke, *Front. Aging Neurosci.* **2016**, *8*, 1663.

[69] H. Bahramali, E. Gordon, J. Lagopoulos, C. L. Lim, W. Li, J. Leslie, J. Wright, *Exp. Aging Res.* **1999**, *25*, 69.

[70] EEG, ECG and pupil data from young and older adults: rest and auditory cued reaction time tasks, https://openneuro.org/datasets/ds003690/versions/1.0.0 (accessed: June 2023).